Taylor & Francis
Taylor & Francis Group

RESEARCH ARTICLE

OPEN ACCESS

Check for updates

Design and synthesis of 1,4,8-triazaspiro[4.5]decan-2-one derivatives as novel mitochondrial permeability transition pore inhibitors

Valentina Albanese[a†], Gaia Pedriali[b†], Martina Fabbri[c], Antonella Ciancetta[c], Silvia Ravagli[c], Chiara Roccatello[c], Remo Guerrini[c,d], Giampaolo Morciano[b,e,f], Delia Preti[c], Paolo Pinton[b,d,e#] and Salvatore Pacifico[c#]

[a]Department of Environmental and Prevention Sciences, University of Ferrara, Ferrara, Italy; [b]Maria Cecilia Hospital, GVM Care & Research, Cotignola, Italy; [c]Department of Chemical, Pharmaceutical and Agricultural Sciences, University of Ferrara, Ferrara, Italy; [d]Technopole of Ferrara, Laboratory for Advanced Therapies (LTTA), Ferrara, Italy; [e]Department of Medical Sciences, Section of Experimental Medicine, University of Ferrara, Ferrara, Italy; [f]Department of Biosciences, Biotechnology and Environment, University of Bari "A. Moro", Bari, Italy

ABSTRACT

Ischaemia/reperfusion injury (IRI) is a condition that occurs when tissues from different organs undergo reperfusion following an ischaemic event. The mitochondrial permeability transition pore (mPTP), a multiprotein platform including structural components of ATP synthase with putative gate function, is an emerging pharmacological target that could be modulated to facilitate the restoration of organ function after a hypoxic insult. Herein, we reported the synthesis and biological characterisation of new molecules with a 1,4,8-triaza-spiro[4.5]decan-2-one framework of potential interest for the treatment of IRI able to inhibit the opening of mPTP in a cardiac model in vitro. Modelling studies were useful to rationalise the observed structure-activity relationship detecting a binding site for the investigated molecules at the interface between the c_8-ring and subunit a of ATP synthase. Compound **14e** was shown to display high potency as mPTP inhibitor combined with the capability to counteract cardiomyocytes death in an in vitro model of hypoxia/reoxygenation.

GRAPHICAL ABSTRACT

Introduction

Reperfusion interventions are the only way to prevent irreversible damage when organs experience ischaemia, for instance during a myocardial or cerebral infarction. However, the efficacy of pharmacological or mechanical reperfusion therapy, even when timely, is reduced by the phenomenon known as ischaemia-reperfusion injury (IRI)[1] which occurs when blood supply to a tissue is restored after an ischaemic insult. Paradoxically, during reperfusion a series of complex mechanisms are known to worsen the initial cellular dysfunction and death. IRI can affect various organs i.e. heart[2], brain[3], kidney[4], and liver[5] with different responses as far as the extent and reversibility of tissue damage thus leading to multiple

pathological conditions, disabilities, and even death. Due to the incomplete understanding of the multifaceted mechanisms behind IRI, the biological bases of these organo-specific differences remain unknown. Consequently, the development of new targeted therapeutic interventions continues to represent an unmet medical need[2,6].

An emerging target in this research field is the so-called mitochondrial permeability transition pore (mPTP) which has been recognised as one of the main responsible for cardiomyocyte death in the final step of IRI in the case of myocardial infarction[7,8]. mPTP is defined as a multiprotein platform at the interface of the inner and outer mitochondrial membranes which includes pore-forming elements and modulators that contribute to the open/closed conformational state[9]. Pore opening mediates mitochondrial permeability transition (MPT)-driven apoptosis, during which the inner mitochondrial membrane, usually highly impermeable, undergoes to a sudden and irreversible increase of permeability. This allows the free entry of all molecules <1.5 kDa into the matrix which translates into ATP depletion, mitochondrial swelling, and release of cytochrome c and other apoptotic proteins ultimately leading to cell death. Of note, the increase of intra-mitochondrial calcium levels and reactive oxygen species occurring in the phase of reperfusion after an ischaemic insult, have been identified as main triggers of mPTP opening.

Several mPTP inhibitors have been identified and mainly explored for their cardioprotective potential. Among these, cyclosporin A (CsA) and TRO40303, have reached clinical studies for the treatment of cardiac IRI[9] but inconsistent results have been achieved as far as their efficacy. It has been suggested that this may be due to the indirect mechanism of action of such drug candidates: CsA is a Cyclophilin D (CypD)-dependent inhibitor while TRO40303 binds the mitochondrial translocator protein (TSPO) located in the outer mitochondrial membrane[10]. Although CypD is still recognised as regulator of mPTP function more than structural components of the pore, several publications have definitively refuted a role for TSPO in the regulation of mPTP[11].

Recent data point to a role for ATP synthase in mPTP formation[12,13]. According to this model, the increase of mitochondrial calcium during reperfusion can convert the energy-supplying ATP synthase machine into an energy-dissipating supramolecular entity[13]. Specifically, independent studies provided evidences that the c subunits of F_1/F_O-ATP synthase play a pivotal role in mPTP formation: depletion of the c subunit reduces channel opening in response to calcium- and oxidative stress-induced stimuli, whereas its over expression enhances mPTP opening[14–17]. The recent disclosure of the Cryo-EM structure of the mammalian F-type ATP synthase provided solid confirmation of the c-ring model[18,19].

In the search for new possible pharmacological approaches for the treatment of IRI, we recently reported the design, synthesis, and structure-activity relationship (SAR) optimisation of mPTP inhibitors targeting the c subunit of F_1/F_O-ATP synthase[20–22]. Among the investigated compounds, a series of spiropiperidine derivatives demonstrated cardioprotective effects in an animal model of IRI. In this study we described our progress in this field leading to the discovery of a novel series of 1,4,8-triazaspiro[4.5]decan-2-one derivatives that were shown to display high *in vitro* potency in inhibiting mPTP opening and cytoprotective activity in an *in vitro* model of hypoxia/reoxygenation. Moreover, modelling studies were useful to rationalise the observed SAR detecting a binding site for the investigated molecules at the interface between the c_8-ring and subunit a of ATP synthase.

Results and discussion

Design and synthesis

Herein, we designed and synthesised new mPTP opening inhibitors basing on a previous series of 1,3,8-triazaspiro[4.5]decane derivatives of which compounds **PP11** and **IB6a** (Figure 1) were shown to display good potency *in vitro*[20]. As simplified analogues of the spirocyclic portion of Oligomycin A and on the base of several experimental evidence, the mechanism of action of these molecules was associated to their capability to target the c subunit of the F_1/F_O-ATP synthase complex thus preventing it to promote the MPT[23]. With the aim of expanding the structure-activity information about these ligands and in the search for even more potent and promising compounds, we decided to synthesise a novel series of spiroimidazolidinones characterised by a 1,4,8-triaza-spiro[4.5]decan-2-one template (Figure 1). The bicyclic core of these compounds, structural isomers of the previous series, was functionalised by introducing different moieties at the 3-position and at the lactam nitrogen. In particular, the imidazolidinone nitrogen was substituted with hydrophilic or salifiable functions with the aim to increase the water solubility and possibly to facilitate formulation in aqueous medium for *in vivo* administration. The chemical space around the 3-position was explored with the introduction of (aryl)alkyl or aryl substituents deriving from the side chain of natural amino acids according to the synthetic approach that has been depicted in Scheme 1.
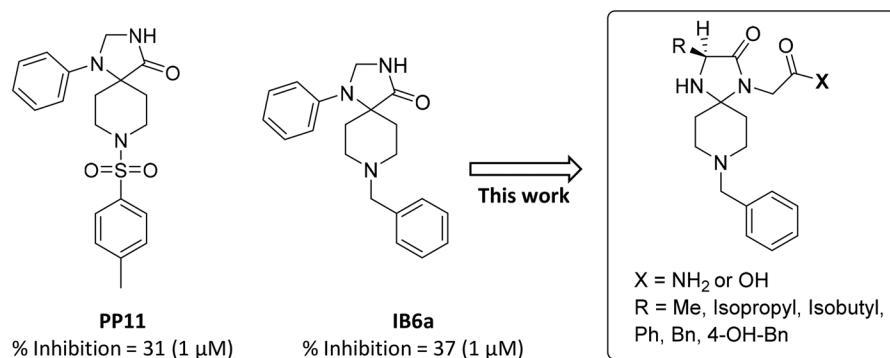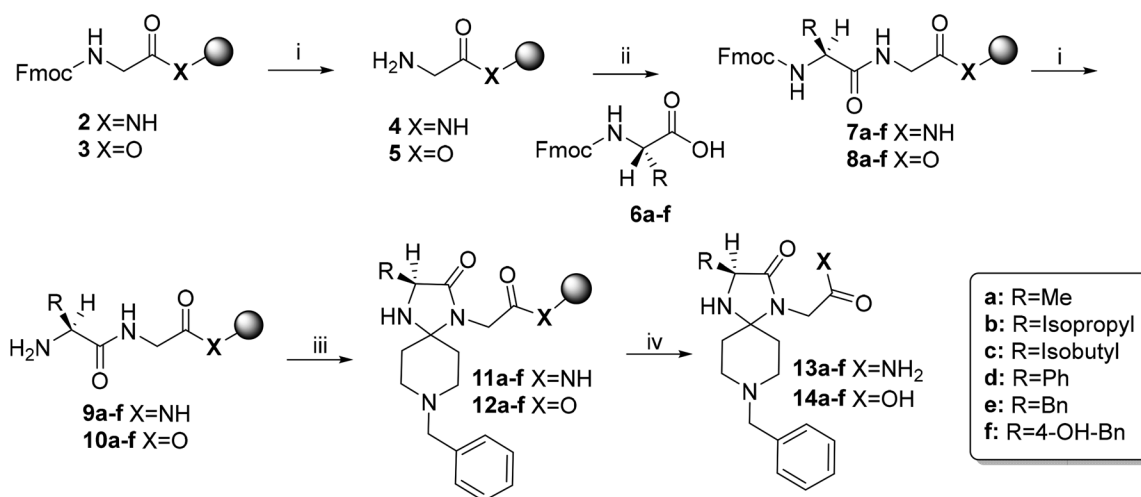
Figure 1. From 1,3,8-triazaspiro[4.5]decane[20] to 1,4,8-triaza-spiro[4.5]decane derivatives as mPTP inhibitors.

Scheme 1. Reagents and conditions: i. 40% piperidine in DMF; ii DIC, HOBt, DMF; iii. N-benzyl-4-piperidone, p-TsOH, toluene, 80 °C, overnight (for **11a-f**) or N-benzyl-4-piperidone, p-TSOH, 2,2-dimethoxypropane, 80 °C, 5h (for **12a-f**); iv. TFA/H$_2$O/Et$_3$SiH (95:2.5:2.5 v/v), rt, 3h.

The target compounds were prepared thanks to the optimisation of a reported solid phase synthesis protocol[24] that has been customised to be accomplished through an automated peptide synthesiser.

A Fmoc-Glycine-Rink amide resin (**2**) or a Fmoc-Glycine-Wang resin (**3**) were employed as starting solid supports which were firstly deprotected with a standard treatment with a solution of piperidine in DMF (40%) and then coupled with the commercially available natural Fmoc-protected amino acids **6a-f**. Following a further Fmoc deprotection step, the resulting dipeptides **9a-f** and **10a-f** were treated at 80 °C with N-benzyl-4-piperidone in different solvents and for different reaction times according to the type of resin used: toluene/overnight in the case of Rink amide resin and 2,2-dimethoxypropane (DMP)/5h for the Wang one. The desired spiropiperidines **13a-f** and **14a-f** were finally cleaved and separated from the solid support by a classical acidic treatment followed by filtration. The use of Rink amide support allowed to obtain amide spirocyclic derivatives while the use of Wang resin led to carboxylic acid spiropiperidines. All the crude products were purified by a semi-preparative

HPLC and a degree of purity higher than 95% have been confirmed by analytic HPLC analysis.

Biological evaluation

In vitro inhibitory activity against mPTP channel opening

The inhibitory activity of compounds **13a-f** and **14a-f** against Ca^{2+}-mediated mPTP opening has been investigated in human ventricular cardiomyocytes (AC16) via the calcein–cobalt (Co^{2+}) assay [25]. Living cells were pre-treated with the potential inhibitors at 1 μM concentration and then ionomycin (1 μM) was added as Ca^{2+} ionophore. The novel compounds along with **PP11** and and **IB6a** employed as internal references[21], were evaluated in triplicate and results are expressed as percentage of mPTP opening inhibition in Table 1.

This preliminary in vitro investigation confirmed the capability of the new spiroimidazolidinone compounds to desensitise mPTP opening with variable potency according to the different substitution pattern (mPTP inhibition ranging from 19% to 43% at 1 μM concentration, excepting **14b** which was inactive).

Table 1. *In vitro* potency of spiro-piperidine derivatives as mPTP opening inhibitors.Calcein – cobalt assay in living human cardiomyocytes (AC16) pre-treated with vehicle (DMSO) or the mPTP inhibitors to be screened. mPTP opening was stimulated by ionomycin administration. The values were expressed as a percentage of the vehicle. Each value is the mean of at least 12 cells from 3 biological and 3 technical replicates.
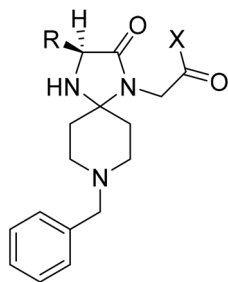
Compd	R	X	mPTP inhibition (%, 1 µM)	Statistic
IB6a	-	-	37	P < 0.0001
PP11	-	-	40,19	P < 0.0001
13a	Me	NH$_2$	18,71	P < 0.001
14a	Me	OH	19,40	P < 0.001
13b	Isopropyl	NH$_2$	28,71	P < 0.0001
14b	Isopropyl	OH	inactive	n.s.
13c	Isobutyl	NH$_2$	29,13	P < 0.0001
14c	Isobutyl	OH	23,01	P < 0.001
13d	Ph	NH$_2$	38,73	P < 0.0001
14d	Ph	OH	36,63	P < 0.0001
13e	Bn	NH$_2$	30,72	P < 0.0001
14e	Bn	OH	43,02	P < 0.0001
13f	4-OH-Bn	NH$_2$	32,17	P < 0.0001
14f	4-OH-Bn	OH	42,11	P < 0.0001

The substituent at the 3-position (R group in Table 1) seems to play a significant role in modulating the inhibitory activity. Indeed, a small methyl group (**13a** and **14a**) promoted a mild inhibitory activity which increases in the presence of more hindered and branched alkyl chains in the acetamides subset (compare **13b** and **13c** to **13a**). The same trend was not observed for the carboxylic acid derivatives among which the isopropyl group determined a complete loss of activity (compare **14a** to **14b**), and the isobutyl chain exerted a comparable effect to that of the methyl group (compare **14a** to **14c**). More potent compounds were obtained by replacing the alkyl moiety at the 3-position with an aryl or an arylalkyl substituent that positively affected the activity of both the acetamide (**13d-f**) and the carboxylic acid (**14d-f**) derivatives. We also evaluated the replacement of the benzyl moiety with a 4-hydroxy benzyl group (compare **13-14e** to **13-14f**) without observing appreciable differences in the biological outcome.

The potencies of amide derivatives were significantly different from those of the corresponding carboxylic acid congeners only in the presence of an isopropyl (**13-14b**), a benzyl (**13-14e**) or a 4-OH-benzyl (**13-14f**) moiety at the 3-position of the bicycle. However, while in the former compounds the presence of an N^1-acetic chain was importantly detrimental for activity (compare **13b** to **14b**), an opposite effect was observed for the latter examples (compare **13e** to **14e** and **13f** to **14f**).

Of the examined molecules **14e**, which combines a C^3-benzyl group with the free carboxylic function at the lactam nitrogen, displayed the highest potency with a similar biological profile compared to PP11.

In vitro evaluation of cytoprotection following hypoxia/reoxygenation

Acute myocardial infarction (MI) is one of the leading causes of death and disability worldwide. The standard treatment of patients with ST-segment-elevation MI (STEMI) for reducing ischaemic injury is the prompt restoration of blood flow via either primary percutaneous coronary intervention or thrombolytic therapy[6]. Even with prompt reperfusion interventions, STEMI still carries a mortality rate of 6–12% and a 1-year prevalence of heart failure ranging from 14–36%. IRI is estimated to account for as much as 50% of the eventual infarct size[26]. Thus, we considered to evaluate the cytoprotective effect of **14e**, the most potent compound of our series, in an *in vitro* model of hypoxia/reoxygenation (H/R) with the AC16 human cardiomyocyte cell line. Figure 2 shows the harmful effects of H/R induction in AC16 cells highlighting about 30% reduction of cell viability in the following 48h of reoxygenation (panel A), probably due to increased cell death (panel B). This data has been confirmed by both fluorescence and biochemical approaches. Treatments of cardiomyocytes with 1 µM **14e** at the time of reoxygenation, significantly increased cell viability by reducing cell death triggered by H/R. Indeed, **14e** inhibited the cleavage of PARP, RIP1 and caspase 3 proteins when administered either for 1h or for 48h, which are effectors of cell death (panel C). The production of reactive oxygen species (ROS) during hypoxia/reoxygenation is recognised as a major contributor to oxidative damage. Although **14e** compound inhibits mPTP it is not able to significantly reduce mitochondrial superoxide generation up to 48h treatment (panel D). Panel E showed mitochondrial membrane potential decreased after H/R and its rescue to control levels at both treatment time points.

Molecular Modelling studies

To rationalise the observed SAR, we docked the newly synthesised compounds at the human ATP Synthase. A preliminary analysis of all available Cryo-EM structures of Sub-region 3 of the Human ATP Synthase[19] was
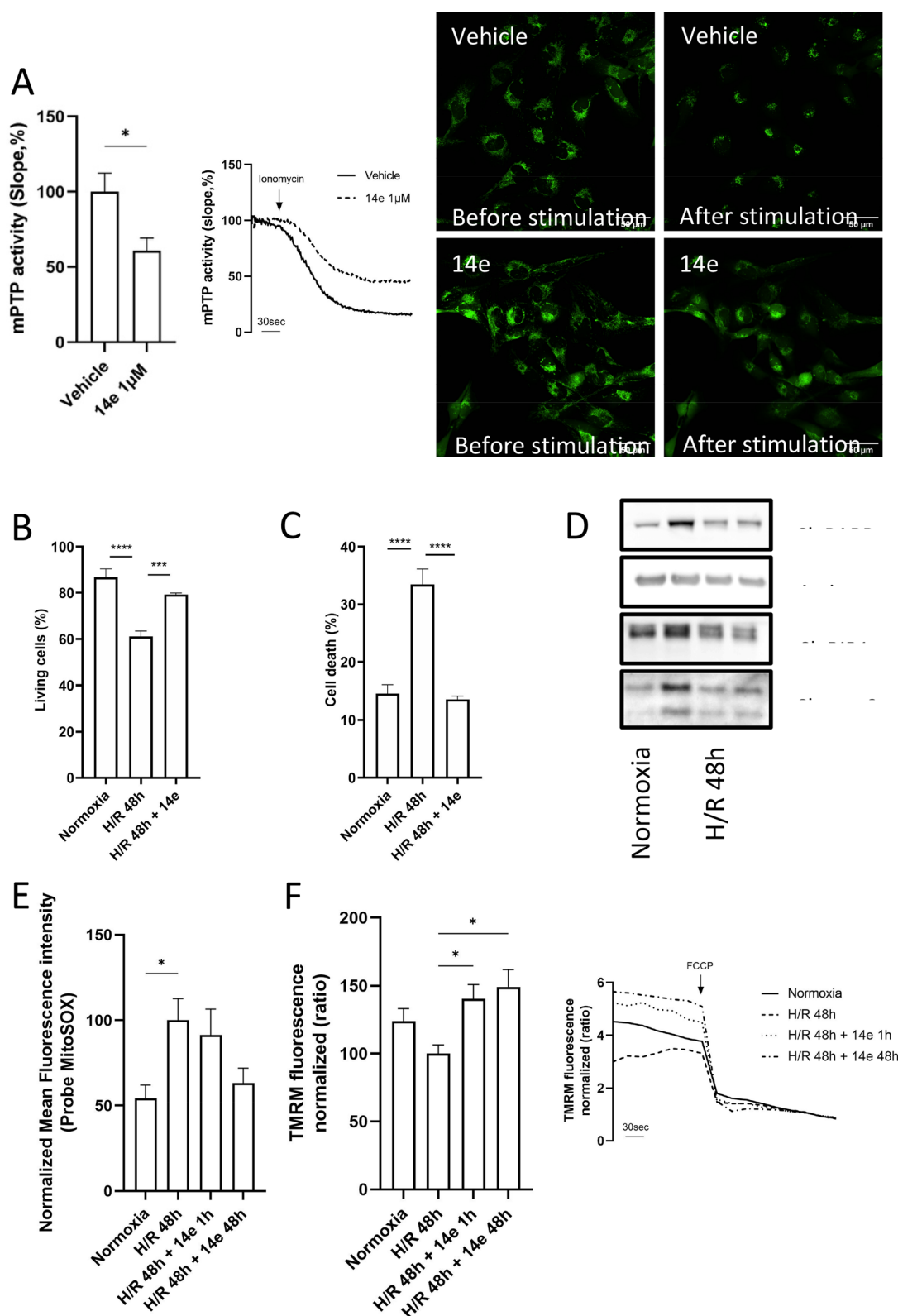
Figure 2. *In vitro* evaluation of H/R damage and **14e**-dependent cytoprotection. A) mPTP activity measured in **14e** treated cells and compared to untreated conditions; representative kinetics and images from confocal microscopy are reported on the right; B) Cytometer-dependent quantification of living cells in percentage. Each value is the mean of 3 biological and 3 technical replicates. C) Quantification of AC16 cells positive to Annexin V staining following H/R. Each value is the mean of 3 biological and 3 technical replicates. D) Immunoblot detection of the main markers of apoptosis and necrosis such as Cleaved PARP, Cleaved Caspase 3 and Cleaved RIP1. This is representative of 3 biological replicates. E) Quantification of the MitoSOX probe intensity in cells following H/R. Each value is the mean of at least 3 biological and 3 technical replicates. F) Quantification of mitochondrial membrane potential and representative kinetics using the TMRM probe, reported as the ratio between the initial intensity and that one reached following 10 nM FCCP administration. Each value is the mean of at least 3 biological and 3 technical replicates. (***) p values < 0.001; (****) p values < 0.0001 (see Figure S1 for raw data).

carried out to identify the structure most suitable for docking. The Site Finder tool as implemented in MOE (Molecular Operating Environment (MOE), 2022.02 Chemical Computing Group ULC, 910–1010 Sherbrooke St. W., Montreal, QC H3A 2R7, 2024) was used to detect a binding site nearby key residues involved in proton translocation in the F_O domain and in particular at the interface between the c_8-ring and subunit a, namely Glu58, Asp224, Tyr221, Asn163 and Arg123. As reported in Table S1, one structure (PDB ID: 8H9M, with Subunit b in the open state termed "3a") features a binding site (Site #3) of appropriate size (146 alpha spheres) and physico-chemical properties to host drug-like molecules (Propensity for Ligand Binding (PLB) index = 2.36[27]) and was therefore selected to carry out the docking analysis. As depicted in Figure 3(A), the binding site lies at the interface between the c_8-ring and helices α5-6 of subunit a. All analogues were docked using the Induced Fit method as implemented in MOE in the so-identified site and the binding poses of compounds displaying mPTP inhibition at 1 μM >30% were carefully inspected. Notably, compounds bearing an aromatic R group at 3-position (**13d-f** and **14d-f**) displayed a common binding mode, that is exemplified by compound **14f** docking pose (Figure 3(B,C)). The

ligand lies with the R group buried at the interface between the c_8-ring and subunit a with the piperidine nitrogen atom and the carboxylic acid function slightly solvent exposed. The benzyl moiety connected to the piperidine nitrogen is hosted in a hydrophobic pocket formed by His127, Y128 and L129 side chains. Two main polar interactions anchor the scaffold in position: a salt-bridge connecting the piperidine nitrogen atom to Asp224 side chain (yellow dashed line in Figure 3(C)), and a H-bond linking the imidazolidinone NH group to Gln152 side chain. In the observed binding poses, the acid/acetamido function does not engage in additional interactions. However, as depicted in Figure 3(C), there is potential for a water mediated electrostatic interaction between the substituent linked to imidazolidinone nitrogen and His223 side chain, as this region is expected to be filled with water molecules passing through the outlet proton translocation half-channel[19]. Interestingly, the proposed binding mode contributes to explain the different inhibition percentage displayed by derivatives bearing alkyl and aryl R groups. As depicted in Figure 3(C), the aromatic substituent can extend towards the bottom of the binding site where Tyr221 and Glu58 are located. As depicted in Figure 3(C) (grey surface) the aromatic ring
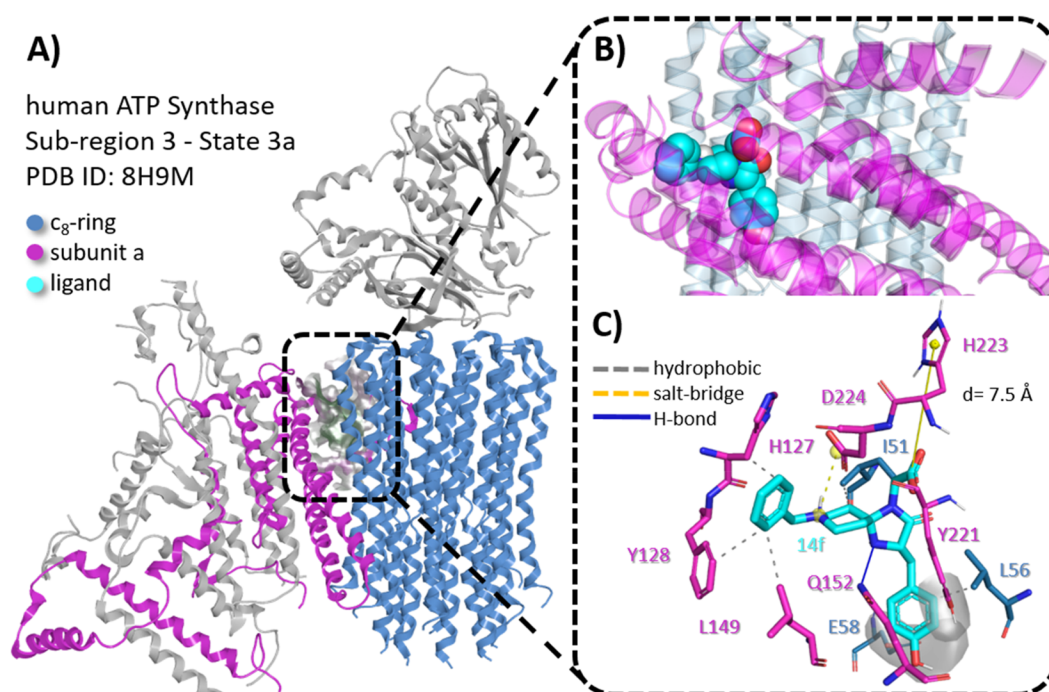

Figure 3. Molecular modelling. A) Location of the detected binding site at the interface between the c_8-ring (light blue cartoon) and helices α5 and α6 of subunit a (magenta cartoon) with respect to the overall human ATP synthase architecture. The site is represented as surface colour coded by lipophilicity with green, grey, and purple representing hydrophobic, neutral and hydrophilic regions, respectively. B) Representative docking pose of compound **14f** (sphere representation, cyan carbon atoms) in the identified binding site. C) Details of established ligand-protein interactions in the predicted binding mode of compound **14f**. Hydrophobic, salt-bridge and H-bond interactions are represented in dashed grey, dashed yellow, and solid blue lines, respectively. The ligand and interaction residues are represented in sticks with ligand carbon atoms in cyan and protein residue carbon atoms colour coded according to the region they belong to as follows: c_8-ring, blue; subunit a, magenta. The grey surface represents the contact surface area between the ligand aromatic R group and protein Tyr221 and Glu58 side chains. Figure in panel A was rendered with MOE, whereas figures in panel B and C were created with PyMOL open source v2.5.0.
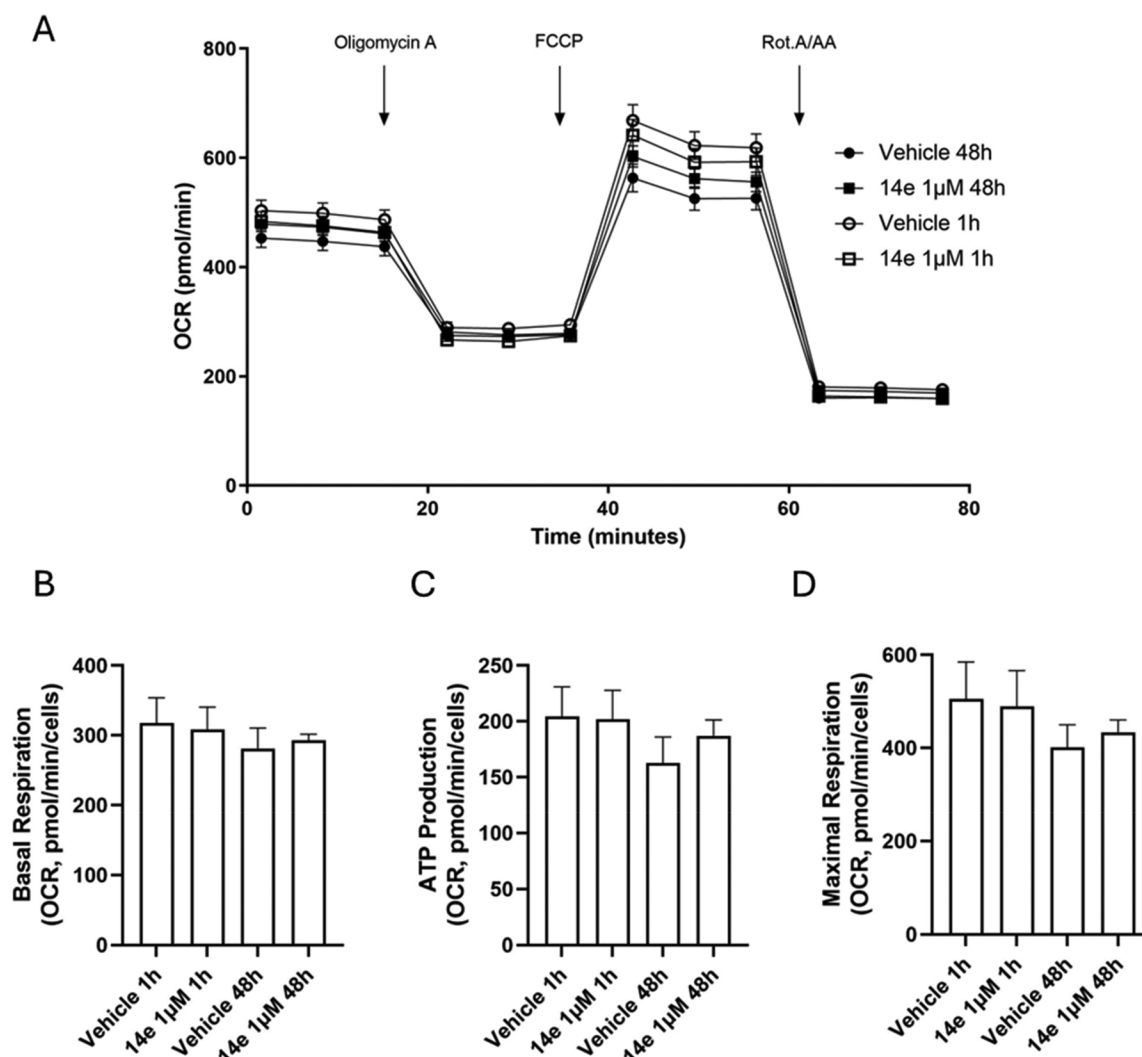
Figure 4. *In vitro* evaluation of the key parameters of mitochondrial respiration. A) Oxygen consumption rate (OCR) kinetics reporting mean values with SEM. B) Statistics for the calculation of basal respiration, C) Statistics for the calculation of ATP-linked respiration. D) Statistics for the calculation of Maximal respiratory capacity. Each value is the mean of at least 3 biological and 3 technical replicates.

with the *para*-OH moiety fits into the narrow binding site floor between the two side chains by putatively preventing the proton translocation in the outlet half-channel. It is indeed conceivable that the OH group mimics/replaces a water molecule that has been detected in the Cryo-EM structure connecting the side chains of the two above-mentioned key residues[19].

In vitro evaluation of mitochondrial respiration after 14e treatment

To exclude side-effects of **14e** treatment on ATP production or respiratory chain activity we assessed mitochondrial oxygen consumption rate (OCR). From the results obtained (Figure 4) we can conclude that **14e** compound does not have a negative significant effect on OCR and ATP. This behaviour is consistent with that observed in our previous series of spiro-piperidine

derivatives targeting the c-subunit, to which compound **14e** is structurally analogous[20].

Conclusion

Behind their cardioprotective properties, mPTP inhibitors hold considerable promise across a range of conditions characterised by mitochondrial dysfunction and cell death such as: stroke, age-related neurodegenerative diseases[27], muscular dystrophies and renal[4] or hepatic[5] IRI. Moreover, inhibiting mPTP could improve the efficacy of organ transplantation and other major surgeries associated with reperfusion injury[28]. Ongoing research and clinical trials are needed to fully realise the therapeutic potential of mPTP inhibitors and ensure their safety and efficacy in human patients. Here we described our advancement in this research area with the development of a new series of compounds among

which **14e** was shown to display high *in vitro* potency in inhibiting mPTP opening and significant cytoprotective activity in an *in vitro* cardiac model of H/R, without affecting ATP production. Modelling studies were useful to rationalise the observed SAR and allowed to detect a binding site for the investigated molecules at the interface between the c_8-ring and subunit a of ATP synthase.

Experimental section

Chemistry

Materials and methods

Enantiopure Fmoc-protected amino acids, resins for SPPS, solvents and all starting materials were purchased from BLDpharm (Kaiserslautern, Germany), Fluorochem and Sigma-Aldrich and used without further purification. SPPS was performed by a Syro XP multiple peptide synthesiser (MultiSynTech GmbH, Witten Germany) using a standard Fmoc/tBu strategy. Final compounds were purified via semi-preparative reverse-phase HPLC using a Waters 600 Multisolvent Delivery System, equipped with a Jupiter column C18 (250×30 mm, 300 Å, 15 μm spherical particle size) and a UV detector set on a wavelength of 220 nm. The column was perfused with a gradient, programmed time by time, of solution A (100% H_2O and 0.1% v/v TFA) and solution B (40% H_2O, 60% CH_3CN and 0.1% v/v TFA) at a flow rate of 20 ml/min. Analytical HPLC analyses were performed on a Beckman 116 liquid chromatograph equipped with a Beckman 166 diode array detector. Analytical purity of the final compounds was assessed using a Phenomenex Kinetex C18 column (150×4.6 mm, 5 μm particle size) and a variable wavelength UV detector set at 220 nm. All final compounds are > 95% pure by HPLC analysis (see supporting information). Analyses were conducted with an eluent consisting of H_2O and CH_3CN, both containing 0.1% v/v TFA, at a flow rate of 0.5 ml/min, using a gradient from 0% to 100% of CH_3CN over 25 min. ^1H NMR and ^{13}C NMR spectra were performed on a Varian 400 MHz spectrometer. The signals were referenced to residual ^1H shift of the deuterated solvents (respectively δ H 7.26 for $CDCl_3$; δ H 2.50 for DMSO-d_6). Chemical shifts (δ) are expressed in parts per million (ppm), using the peak of tetramethylsilane as an internal standard in deuterated solvents, while values of coupling constants (*J*) are reported in Hertz (Hz). Splitting patterns are designed as s, singlet; d, doublet; t, triplet; q, quartette; m, multiplet; and b, broad.

General synthetic procedures

Fmoc-Gly-Rink amide resin (**2**, 0.11 mmol, 200 mg, loading 0.55 mmol/g) and Fmoc-Gly-Wang resin (**3**, 0.2 mmol, 200 mg, loading: 1.0 mmol/g) were swollen in anhydrous DMF (*N,N′*-dimethylformamide) for 30 min and employed as starting material for the preparation of all the final compounds.

General procedure for the synthesis of 4, 5, 9a-f and 10a-f (Fmoc deprotection)

N-Fmoc removal from **2**, **3**, and **7a-f** and **8a-f** was performed by two consecutive treatments of the resin with a 40% solution of piperidine in DMF (2 ml/0.2 g of resin) for 5 min. The reaction leading to **7a-f** and **8a-f** was monitored by a micro-cleavage using the cocktail mixture of TFA/H_2O/Et_3SiH (95:2.5:2.5) followed by ESI-MS analysis. Solvent was filtered out and the resin was washed five times with fresh DMF (2 ml/0.2 g of resin) before the next step.

General procedure for the synthesis of 7a-f and 8a-f (amide coupling reaction)

The unprotected glycine residue anchored to a Rink amide (**4**) or a Wang (**5**) resin was coupled with the Fmoc protected amino acids **6a-f** (0.5 M) using HOBt (0.78 M) and DIC (1.09 M) in DMF (1.1:0.7:0.5 v/v; 2.3 ml/0.2 g of resin) as coupling reagents. The reaction was monitored by a micro-cleavage using the cocktail mixture of TFA/H_2O/Et_3SiH (95:2.5:2.5) followed by ESI-MS analysis. Solvent was filtered out and the resin was washed five times with fresh DMF (2 ml/0.2 g of resin) before the next step.

General procedure for the synthesis of 11a-f

To a solution of *N*-benzyl-4-piperidone (30.60 μL, 0.11 mmol) in toluene (4 ml), were consecutively added a catalytic amount of p-toluenesulfonic acid monohydrate (0.2 mg, 0.0011 mmol) and the free *N*-terminal dipeptide anchored to the Rink Amide Resin (**9a-f**, 200 mg, 0.11 mmol). The reaction mixture was slowly stirred overnight at 80 °C. The reaction was monitored by a micro-cleavage using the cocktail mixture of TFA/H_2O/Et_3SiH (95:2.5:2.5) followed by ESI-MS analysis. The solvent was filtered out and the solid support was washed with DMF (5×2 ml) and subsequentially with CH_2Cl_2 (3×2 ml).

General procedure for the synthesis of 12a-f

To a solution of *N*-benzyl-4-piperidone (37 μL, 0.2 mmol) in 2,2-dimethoxypropane (4 ml), were consecutively added a catalytic amount of p-toluenesulfonic acid monohydrate (0.3 mg, 0.002 mmol) and free *N*-terminal

dipeptide anchored to the Wang resin (**10a-f**, 200 mg, 0.2 mmol). The reaction mixture was slowly stirred for 5 h at 80 °C. The reaction was monitored by a micro-cleavage using a cocktail mixture of TFA/H_2O/Et₃SiH (95:2.5:2.5) followed by ESI-MS analysis. The solvent was filtered out and the solid support was firstly washed with DMF (5×2 ml) and finally with CH_2Cl_2 (3×2 ml).

General procedure for the synthesis of 13a-f and 14a-f

The final spiro derivatives anchored to the solid support (**11a-f** and **12a-f**), were treated with a cleavage solution composed by TFA, H_2O and Et₃SiH (95:2.5:2.5 v/v; 10 ml/0.2 g of resin) for 3 h at room temperature. After filtration of the exhausted resin, volatiles were removed under vacuum, and from the resulting residue a solid was suspended in diethyl ether (Et₂O), isolated through centrifugation and finally purified by reversed-phase semi-preparative HPLC.

(S)-2–(8-benzyl-3-methyl-2-oxo-1,4,8-triazaspiro[4.5]decan-1-yl)acetamide (13a): Yellow oil (yield 38%). ^1H NMR (400 MHz, DMSO-d₆) δ 9.51 (bs, 1H), 7.55–7.43 (m, 6H), 7.34 (s, 1H), 7.12 (s, 1H), 4.33 (s, 2H), 3.71 (d, J=17.1 Hz, 1H), 3.63–3.04 (m, 6H), 2.16–2.05 (m, 1H), 1.97–1.67 (m, 3H), 1.19 (d, J=6.9 Hz, 3H). ^{13}C NMR (101 MHz, DMSO-d₆) δ 175.14, 169.31, 131.12, 131.10, 129.53, 128.80, 73.55, 58.59, 52.40, 48.73, 48.04, 41.92, 31.72, 29.24, 16.17. MS (ESI): calculated for $C_{17}H_{25}N_4O_2$ $[M+H]^+$ 317.4125; found 317.1975. HPLC: t_R = 10.69 min.

(S)-2–(8-benzyl-3-methyl-2-oxo-1,4,8-triazaspiro[4.5]decan-1-yl)acetic acid (14a): Yellow oil (yield 28%). ^1H NMR (400 MHz, DMSO-d₆) δ 9.62 (bs, 1H), 7.61–7.38 (m, 6H), 4.34 (s, 2H), 3.86–3.67 (m, 2H), 3.51–3.06 (m, 7H), 2.26–2.09 (m, 1H), 2.04–1.62 (m, 3H), 1.18 (d, J=6.9 Hz, 3H). ^{13}C NMR (101 MHz, DMSO-d₆) δ 175.60, 170.49, 131.66, 131.62, 130.08, 129.37, 74.05, 59.13, 52.86, 49.26, 48.58, 41.31, 32.41, 30.22, 17.07. MS (ESI): calculated for $C_{17}H_{24}N_3O_3$ $[M+H]^+$ 318.1812; found 318.2321. HPLC: t_R = 11.50 min.

(S)-2–(8-benzyl-3-isopropyl-2-oxo-1,4,8-triazaspiro[4.5]decan-1-yl)acetamide (13b): Yellow oil (yield 31%). ^1H NMR (400 MHz, DMSO-d₆) δ 9.38 (bs, 1H), 7.53–7.43 (m, 6H), 7.33 (s, 1H), 7.06 (s, 1H), 4.33 (s, 2H), 3.69 (d, J=17.1 Hz, 1H), 3.56 (d, J=17.1 Hz, 1H), 3.38–3.13 (m, 5H), 2.08–1.80 (m, 3H), 1.72–1.60 (m, 2H), 0.96 (d, J=6.8 Hz, 3H), 0.85 (d, J=6.8 Hz, 3H). ^{13}C NMR (101 MHz, DMSO-d₆) δ 174.01, 169.60, 131.64, 130.23, 130.10, 129.36, 73.51, 62.34, 59.23, 49.19, 48.93, 42.06, 33.20, 31.43, 29.86, 19.69, 18.13. MS (ESI): calculated for $C_{19}H_{29}N_4O_2$ $[M+H]^+$ 345.4665; found 345.4126. HPLC: t_R = 11.15 min.

(S)-2–(8-benzyl-3-isopropyl-2-oxo-1,4,8-triazaspiro[4.5]decan-1-yl)acetic acid (14b): Orange oil (yield 15%). ^1H NMR (400 MHz, DMSO-d₆) δ 9.39 (bs, 1H), 7.52–7.43 (m, 6H), 4.33 (s, 2H), 3.85 (d, J=17.8 Hz, 1H), 3.67 (d, J=17.8 Hz, 1H), 3.36–3.15 (m, 5H), 2.13–1.83 (m, 3H), 1.72–1.61 (m, 2H), 0.96 (d, J=6.8 Hz, 3H), 0.84 (d, J=6.8 Hz, 3H). ^{13}C NMR (101 MHz, DMSO-d₆) δ 173.95, 170.38, 131.62, 130.23, 130.10, 129.37, 73.46, 62.25, 59.27, 49.20, 48.93, 41.05, 33.28, 31.50, 29.91, 19.59, 17.84. MS (ESI): calculated for $C_{19}H_{28}N_3O_3$ $[M+H]^+$ 346.2125; found 346.2477. HPLC: t_R = 13.57 min.

(S)-2–(8-benzyl-3-isobutyl-2-oxo-1,4,8-triazaspiro[4.5]decan-1-yl)acetamide (13c): Yellow oil (yield 30%). ^1H NMR (400 MHz, DMSO-d₆) δ 9.36 (bs, 1H), 7.57–7.42 (m, 6H), 7.32 (s, 1H), 7.11 (s, 1H), 4.34 (s, 2H), 3.69 (d, J=17.1 Hz, 1H), 3.53 (d, J=17.1 Hz, 1H), 3.47–3.06 (m, 5H), 2.16–1.99 (m, 1H), 1.98–1.70 (m, 4H), 1.57–1.47 (m, 1H), 1.37–1.27 (m, 1H), 0.91 (d, J=6.7 Hz, 3H), 0.87 (d, J=6.7 Hz, 3H). ^{13}C NMR (101 MHz, DMSO-d₆) δ 175.67, 169.87, 131.62, 130.27, 130.08, 129.35, 74.25, 59.19, 55.67, 49.39, 48.88, 42.39, 40.94, 32.56, 30.24, 25.08, 23.67, 21.86. MS (ESI): calculated for $C_{20}H_{31}N_4O_2$ $[M+H]^+$ 359.4935; found 359.3998. HPLC: t_R = 12.23 min.

(S)-2–(8-benzyl-3-isobutyl-2-oxo-1,4,8-triazaspiro[4.5]decan-1-yl)acetic acid (14c): Orange oil (yield 29%). ^1H NMR (400 MHz, DMSO-d₆) δ 9.35 (bs, 1H), 7.55–7.42 (m, 6H), 4.34 (s, 2H), 3.83 (d, J=17.8 Hz, 1H), 3.70 (d, J=17.8 Hz, 1H), 3.46–3.01 (m, 6H), 2.14–2.04 (m, 1H), 2.00–1.60 (m, 3H), 1.55–1.44 (m, 1H), 1.32–1.21 (m, 1H), 0.91 (d, J=6.7 Hz, 3H), 0.87 (d, J=6.7 Hz, 3H). ^{13}C NMR (101 MHz, DMSO-d₆) δ 175.69, 170.52, 131.61, 130.30, 130.08, 129.35, 74.14, 59.18, 55.59, 49.39, 48.93, 41.28, 40.17, 32.77, 30.62, 25.04, 23.68, 21.82. MS (ESI): calculated for $C_{20}H_{30}N_3O_3$ $[M+H]^+$ 360.2282; found 360.3399. HPLC: t_R = 14.82 min.

(S)-2–(8-benzyl-2-oxo-3-phenyl-1,4,8-triazaspiro[4.5]decan-1-yl)acetamide (13d): Yellow oil (yield 41%). ^1H NMR (400 MHz, DMSO-d₆) δ 9.53 (bs, 1H), 7.53–7.39 (m, 8H), 7.37–7.23 (m, 4H), 7.11 (s, 1H), 4.63 (s, 1H), 4.34 (s, 2H), 3.72–3.68 (m, 2H), 3.49–3.12 (m, 4H), 2.20–1.95 (m, 2H), 1.89 (d, J=13.2 Hz, 1H), 1.72 (d, J=13.2 Hz, 1H). ^{13}C NMR (101 MHz, DMSO-d₆) δ 173.24, 169.56, 139.25, 131.68, 130.13, 130.10, 129.36, 128.54, 128.14, 127.87, 74.13, 60.85, 59.27, 49.11, 48.82, 42.44, 33.10, 31.25. MS (ESI): calculated for $C_{22}H_{27}N_4O_2$ $[M+H]^+$ 379,2129; found 379.3060. HPLC: t_R = 11.86 min.

(S)-2–(8-benzyl-2-oxo-3-phenyl-1,4,8-triazaspiro[4.5]decan-1-yl)acetic acid (14d): Orange oil (yield 28%). ^1H NMR (400 MHz, DMSO-d₆) δ 9.61 (bs, 1H), 7.56–7.38 (m, 8H), 7.38–7.24 (m, 3H), 4.64 (s, 1H), 4.34 (s, 2H), 3.94–3.74 (m, 2H), 3.42–3.20 (m, 4H), 2.21–2.04 (m, 2H), 1.87 (d, J=13.8 Hz, 1H), 1.72 (d, J=13.8 Hz, 1H). ^{13}C NMR (101 MHz, DMSO-d₆) δ 173.13, 170.34, 139.24, 131.66,

130.14, 130.09, 129.36, 128.59, 128.13, 127.94, 74.06, 60.82, 59.27, 49.06, 48.81, 41.42, 40.59, 33.15, 31.31. MS (ESI): calculated for $C_{22}H_{26}N_3O_3$ $[M+H]^+$ 380.1969; found 380.1863. HPLC: t_R = 14.85 min.

(S)-2–(3,8-dibenzyl-2-oxo-1,4,8-triazaspiro[4.5] decan-1-yl)acetamide (13e): Pale white solid (yield 35%). ^{1}H NMR (400 MHz, DMSO-d$_6$) δ 9.37 (bs, 1H), 7.52–7.41 (m, 6H), 7.35 (s, 1H), 7.32–7.09 (m, 6H), 4.31 (s, 2H), 3.73–3.54 (m, 3H), 3.39–2.98 (m, 5H), 2.72–2.62 (m, 1H), 2.08–1.86 (m, 2H), 1.74 (d, J=13.6 Hz, 1H), 1.58 (d, J=13.6 Hz, 1H). ^{13}C NMR (101 MHz, DMSO-d$_6$) δ 174.69, 169.76, 139.36, 131.63, 130.24, 130.06, 129.60, 129.32, 128.62, 126.60, 74.34, 59.21, 59.04, 49.17, 48.85, 42.44, 38.06, 32.60, 30.71. MS (ESI): calculated for $C_{23}H_{29}N_4O_2$ $[M+H]^+$ 393,2285; found 393.4768. HPLC: t_R = 12.93 min.

(S)-2–(3,8-dibenzyl-2-oxo-1,4,8-triazaspiro[4.5] decan-1-yl)acetic acid (14e): Yellow oil (yield 28%). ^{1}H NMR (400 MHz, DMSO-d$_6$) δ 12.85 (s, 1H), 9.40 (s, 1H), 7.53–7.41 (m, 5H), 7.32–7.16 (m, 6H), 4.32 (s, 2H), 3.83–3.65 (m, 2H), 3.40–2.96 (m, 6H), 2.68–2.61 (m, 1H), 2.14–1.90 (m, 2H), 1.72 (d, J=13.3 Hz, 1H), 1.55 (d, J=13.3 Hz, 1H). ^{13}C NMR (101 MHz, DMSO-d$_6$) δ 174.52, 170.40, 139.20, 131.61, 130.24, 130.06, 129.65, 129.32, 128.59, 126.61, 74.28, 59.08, 59.06, 49.12, 48.88, 41.33, 38.27, 32.78, 30.97. MS (ESI): calculated for $C_{23}H_{28}N_3O_3$ $[M+H]^+$ 394.2125; found 394.3277. HPLC: t_R = 20.05 min.

(S)-2–(8-benzyl-3–(4-hydroxybenzyl)-2-oxo-1,4,8-triazaspiro[4.5]decan-1-yl)acetamide (13f): Yellow oil (yield 34%). ^{1}H NMR (400 MHz, DMSO-d$_6$) δ 9.36 (bs, 1H), 7.54–7.39 (m, 6H), 7.32 (s, 1H), 7.12 (s, 1H), 7.04 (d, J=8.2 Hz, 2H), 6.65 (d, J=8.2 Hz, 2H), 4.31 (s, 2H), 3.66–3.56 (m, 3H), 3.37–3.01 (m, 4H), 2.93–2.87 (m, 1H), 2.62–2.54 (m, 1H), 2.07–1.86 (m, 2H), 1.73 (d, J=12.8 Hz, 1H), 1.51 (d, J=12.8 Hz, 1H). ^{13}C NMR (101 MHz, DMSO-d$_6$) δ 174.78, 169.78, 156.19, 131.62, 130.51, 130.23, 130.05, 129.32, 129.18, 115.38, 74.27, 59.42, 59.08, 49.18, 48.87, 42.43, 37.15, 32.61, 30.79. MS (ESI): calculated for $C_{23}H_{29}N_4O_3$ $[M+H]^+$ 409.2234; found 409.3512. HPLC: t_R = 10.98 min.

(S)-2–(8-benzyl-3–(4-hydroxybenzyl)-2-oxo-1,4,8-triazaspiro[4.5]decan-1-yl)acetic acid (14f): Yellow oil (yield 28%). ^{1}H NMR (400 MHz, DMSO-d$_6$) δ 9.45 (bs, 1H), 7.58–7.37 (m, 6H), 7.04 (d, J=8.5 Hz, 2H), 6.65 (d, J=8.5 Hz, 2H), 4.31 (s, 2H), 3.80–3.76 (m, 1H), 3.63–3.57 (m, 2H), 3.37–3.03 (m, 4H), 2.93–2.85 (m, 1H), 2.60–2.52 (m, 1H), 2.14–1.88 (m, 2H), 1.70 (d, J=13.4 Hz, 1H), 1.49 (d, J=13.4 Hz, 1H). ^{13}C NMR (101 MHz, DMSO-d$_6$) δ 174.62, 170.41, 156.20, 131.60, 130.56, 130.25, 130.05, 129.32, 129.01, 115.37, 74.20, 59.30, 59.07, 49.11, 48.87, 41.29, 37.32, 32.76, 31.02. MS (ESI): calculated for $C_{23}H_{28}N_3O_4$ $[M+H]^+$ 410.2074; found 410.5575. HPLC: t_R = 11.24 min.

Biological assays

Immunoblot assay

For immunoblotting, cells were lysed in RIPA buffer, protein was quantified by the Lowry method, and 15 µg of protein was loaded into each slot of a 4–20% precast gel. After electrophoretic separation, proteins were transferred onto nitrocellulose membranes that were incubated overnight with the following primary antibodies: actin (as loading marker), cleaved RIP1, cleaved caspase 3 and cleaved PARP. Protein expression was assessed by specific HRP-labeled secondary antibodies, followed by detection by chemiluminescence.

Calcein-cobalt assay

AC16 cells were pre-treated with DMSO (vehicle) and compounds for 15 min. For all the experiments the compounds were used 1 µM. Cells were loaded with calcein acetoxymethyl ester and Co^{2+} as previously described[25]. Staining solution was added to the cells for 15 min at 37 °C in a 5% CO_2 atmosphere. Image acquisitions were performed with a motorised Nikon AXE R confocal microscope with a 40X/0.6 PlanApo objective and laser LU-N4S 405/488/561/640. Ionomycin (1 µM) was administered 30 s after the beginning of the experiment to induce mPTP opening.

Mitochondrial membrane potential assay

Cells were loaded with 20 nM tetramethylrhodamine methyl ester (TMRM) for 30 min at 37 °C. To obtain and analyse basal levels, cells were stimulated with 10 nM carbonyl cyanide p-trifluoromethoxyphenylhydrazone (FCCP), a strong uncoupler of oxidative phosphorylation. Image acquisitions were performed with a motorised Nikon AXE R confocal microscope with a 40X/0.6 PlanApo objective and laser LU-N4S 405/488/561/640.

ROS measurements

ROS measurements were performed according to what described by Wojtala and co-worker[29]. Briefly, measurement of mitochondrial superoxide ($mtO_2 \bullet^-$) production was performed on cells incubated for 30 min at 37 °C in the presence of 5 µM mitoSOX red. A counterstaining with MitoTracker Deep Red has been performed in order to quantify mitoSOX red fluorescence intensity specifically at mitochondria. The fluorescence was evaluated on Nikon AXE R confocal microscope with a PlanApo 60X/1.4 objective and laser LU-N4S 405/488/561/640.

Annexin V assay

The AC16 human cardiomyocyte cell line was purchased from Sigma Aldrich (code SCC109). Cells were

gently harvested by centrifugation, resuspended in 500 µl of 1X Binding Buffer, 5 µl of Annexin V-FITC has been added followed by 5 min room temperature incubation in the dark, according to the manufacturer's protocol (Biovision, Milpitas, CA, USA). Annexin V Detection Kit is based on the observation that soon after initiating apoptosis, cells translocate the membrane phosphatidylserine (PS) from the inner face of the plasma membrane to the cell surface. Once on the cell surface, PS can be easily detected by staining with a fluorescent conjugate of Annexin V, a protein that has a high affinity for PS. So, the green fluorescence signal was quantified under all conditions on a Tali image-based cytometer (Invitrogen). Cells not positive to Annexin V staining have been considered as living cells. Data are shown as percentage.

Statistical analysis

The statistical method used is one-way ANOVA with multiple comparisons performed by GraphPad Prism 9 (Prism, La Jolla, CA, USA). A p values <0.05 was considered significant. P values are reported in the figure legends.

Molecular Modelling

Binding site detection

All Cryo-EM structures of subregion 3 of the human ATP Synthase available to date were retrieved from the Protein Data Bank[30] (PDB IDs: 8H9F, 8H9J, 8H9M, 8H9Q[19]) and prepared for subsequent analysis by adding Hydrogen atoms and reconstructing missing side chains with the QuickPrep module as implemented in the MOE suite (Molecular Operating Environment (MOE), 2022.02 Chemical Computing Group ULC, 910–1010 Sherbrooke St. W., Montreal, QC H3A 2R7, 2024). Missing protein portions and loops were not modelled and site mutations engineered in the Cryo-EM construct were kept as they are not located in the proximity of the region of interest. Binding cavities at the interface between the c_8-ring and subunit a in the F_o domain were identified with MOE Site Finder module and the alpha spheres comprised in Site 4 in the structure with PDB ID: 8H9M were used to define the binding site centre for the docking calculations.

Docking & data analysis

All newly synthesised analogues were docked at Site 4 with MOE Dock: Up to 30 poses were generated with the default Triangle Matcher placement method and refined via the Induced Fit procedure by saving up to 5 poses for compound. Although compounds displaying higher inhibition percentage returned on average more favourable docking scores, pose selection was based on an agreement between the ligand orientation and the binding site shape and number of ligand-protein interactions detected rather than the docking score. A consensus binding mode for the analogues was selected based on the best consensus pose of the most active compounds with % inhibition > 30%, namely **13d-f** and **14d-f**. Modelling pictures were generated with MOE and PyMOL Open Source v. 2.5.0 (The PyMOL Molecular Graphics System, Schrödinger, LLC) and protein-ligand interactions detected with PLIP[31].

Author contributions

Conceptualisation: D.P., P.P., R.G., G.M.; *In vitro* experiments: G.M., G.P.; chemical synthesis data: S.P., V.A., S.R., C.R., M.F; Molecular Modelling data: A.C.; writing—original draft preparation: D.P, G.M, S.P. All authors have approved the final version of the manuscript.

Disclosure statement

No potential conflict of interest was reported by the author(s).

Data availability statement

The data that support the findings of this study are available from the corresponding authors, [D.P; G.M.], upon reasonable request.

References

1. Zhang M, Liu Q, Meng H, Duan H, Liu X, Wu J, Gao F, Wang S, Tan R, Yuan J. Ischemia-reperfusion injury: molecular mechanisms and therapeutic targets. Signal Transduct Target Ther. 2024;9(1):12.
2. Heusch G. Myocardial ischaemia-reperfusion injury and cardioprotection in perspective. Nat Rev Cardiol. 2020;17(12):773–789.

3. Pan J, Konstas AA, Bateman B, Ortolano GA, Pile-Spellman J. Reperfusion injury following cerebral ischemia: pathophysiology, MR imaging, and potential therapies. Neuroradiology. 2007;49(2):93–102.

4. Shiva N, Sharma N, Kulkarni YA, Mulay SR, Gaikwad AB. Renal ischemia/reperfusion injury: An insight on in vitro and in vivo models. Life Sci. 2020;256:117860.

5. Konishi T, Lentsch AB. Hepatic ischemia/reperfusion: mechanisms of tissue injury, repair, and regeneration. Gene Expr. 2017;17(4):277–287.

6. Fröhlich GM, Meier P, White SK, Yellon DM, Hausenloy DJ. Myocardial reperfusion injury: looking beyond primary PCI. Eur Heart J. 2013;34(23):1714–1722.

7. Bonora M, Giorgi C, Pinton P. Molecular mechanisms and consequences of mitochondrial permeability transition. Nat Rev Mol Cell Biol. 2022;23(4):266–285.

8. Pedriali G, Ramaccini D, Bouhamida E, Wieckowski MR, Giorgi C, Tremoli E, Pinton P. Perspectives on mitochondrial relevance in cardiac ischemia/reperfusion injury. Front Cell Dev Biol. 2022;10:1082095.

9. Briston T, Selwood DL, Szabadkai G, Duchen MR. Mitochondrial permeability transition: a molecular lesion with multiple drug targets. Trends Pharmacol Sci. 2019;40(1):50–70.

10. Morin D, Musman J, Pons S, Berdeaux A, Ghaleh B. Mitochondrial translocator protein (TSPO): From physiology to cardioprotection. Biochem Pharmacol. 2016;105:1–13.

11. Šileikytė J, Blachly-Dyson E, Sewell R, Carpi A, Menabò R, Di Lisa F, Ricchelli F, Bernardi P, Forte M. Regulation of the mitochondrial permeability transition pore by the outer membrane does not involve the peripheral benzodiazepine receptor (Translocator Protein of 18 kDa (TSPO)). J Biol Chem. 2014;289(20):13769–13781.

12. Mnatsakanyan N, Llaguno MC, Yang Y, Yan Y, Weber J, Sigworth FJ, Jonas EA. A mitochondrial megachannel resides in monomeric F1FO ATP synthase. Nat Commun. 2019;10(1):5823.

13. Urbani A, Giorgio V, Carrer A, Franchin C, Arrigoni G, Jiko C, Abe K, Maeda S, Shinzawa-Itoh K, Bogers JFM, et al. Purified F-ATP synthase forms a Ca2+-dependent high-conductance channel matching the mitochondrial permeability transition pore. Nat Commun. 2019;10(1):4341.

14. Bonora M, Bononi A, De Marchi E, Giorgi C, Lebiedzinska M, Marchi S, Patergnani S, Rimessi A, Suski JM, Wojtala A, et al. Role of the c subunit of the FO ATP synthase in mitochondrial permeability transition. Cell Cycle. 2013;12(4):674–683. Feb 15

15. Alavian KN, Beutner G, Lazrove E, Sacchetti S, Park HA, Licznerski P, Li H, Nabili P, Hockensmith K, Graham M, et al. An uncoupling channel within the c-subunit ring of the F1FO ATP synthase is the mitochondrial permeability transition pore. Proc Natl Acad Sci U S A. 2014;111(29):10580–10585. Jul 22

16. Bonora M, Morganti C, Morciano G, Pedriali G, Lebiedzinska-Arciszewska M, Aquila G, Giorgi C, Rizzo P, Campo G, Ferrari R, et al. Mitochondrial permeability transition involves dissociation of F1FO ATP synthase dimers and C-ring conformation. EMBO Rep. 2017;18(7):1077–1089. Jul

17. Morciano G, Pedriali G, Bonora M, Pavasini R, Mikus E, Calvi S, Bovolenta M, Lebiedzinska-Arciszewska M, Pinotti M, Albertini A, et al. A naturally occurring mutation in ATP synthase subunit c is associated with increased damage following hypoxia/reoxygenation in STEMI patients. Cell Rep. 2021;35(2):108983. Apr 13

18. Pinke G, Zhou L, Sazanov LA. Cryo-EM structure of the entire mammalian F-type ATP synthase. Nat Struct Mol Biol. 2020;27(11):1077–1085.

19. Lai Y, Zhang Y, Zhou S, Xu J, Du Z, Feng Z, Yu L, Zhao Z, Wang W, Tang Y, et al. Structure of the human ATP synthase. Mol Cell. 2023;83(12):2137–2147.e4.

20. Morciano G, Preti D, Pedriali G, Aquila G, Missiroli S, Fantinati A, Caroccia N, Pacifico S, Bonora M, Talarico A, et al. Discovery of novel 1,3,8-Triazaspiro[4.5]decane derivatives that target the c subunit of F1/FO-adenosine triphosphate (ATP) synthase for the treatment of reperfusion damage in myocardial infarction. J Med Chem. 2018;61(16):7131–7143.

21. Fantinati A, Morciano G, Turrin G, Pedriali G, Pacifico S, Preti D, Albanese V, Illuminati D, Cristofori V, Giorgi C, et al. Identification of small-molecule urea derivatives as PTPC modulators targeting the c subunit of F1/Fo-ATP synthase. Bioorg Med Chem Lett. 2022;72:128822. Sep 15

22. Turrin G, Lo Cascio E, Giacon N, Fantinati A, Cristofori V, Illuminati D, Preti D, Morciano G, Pinton P, Agyapong ED, et al. Spiropiperidine-based oligomycin-analog ligands to counteract the ischemia-reperfusion injury in a renal cell model. J Med Chem. 2024;67(1):586–602.

23. Pedriali G, Ramaccini D, Bouhamida E, Branchini A, Turrin G, Tonet E, Scala A, Patergnani S, Pinotti M, Trapella C, et al. 1,3,8-triazaspiro[4.5]decane derivatives inhibit permeability transition pores through a FO-ATP synthase c subunit glu119-independent mechanism that prevents oligomycin a-related side effects. Int J Mol Sci. 2023;24(7):6191.

24. Feliu L, Subra G, Martinez J, Amblard M. Spiroimidazolidinone library derivatives on SynPhase lanterns. J Comb Chem. 2003;5(4):356–361.

25. Bonora M, Morganti C, Morciano G, Giorgi C, Wieckowski MR, Pinton P. Comprehensive analysis of mitochondrial permeability transition pore activity in living cells using fluorescence-imaging-based techniques. Nat Protoc. 2016;11(6):1067–1080.

26. Rout A, Tantry US, Novakovic M, Sukhi A, Gurbel PA. Targeted pharmacotherapy for ischemia reperfusion injury in acute myocardial infarction. Expert Opin Pharmacother. 2020;21(15):1851–1865.

27. Kalani K, Yan SF, Yan SS. Mitochondrial permeability transition pore: a potential drug target for neurodegeneration. Drug Discov Today. 2018;23(12):1983–1989.

28. Fernández AR, Sánchez-Tarjuelo R, Cravedi P, Ochando J, López-Hoyos M. Review: Ischemia Reperfusion Injury-A Translational Perspective in Organ Transplantation. Int J Mol Sci. 2020;21(22):8549.

29. Wojtala A, Bonora M, Malinska D, Pinton P, Duszynski J, Wieckowski MR. Methods to monitor ROS production by fluorescence microscopy and fluorometry. Methods Enzymol. 2014;542:243–262.

30. Berman HM, Westbrook J, Feng Z, Gilliland G, Bhat TN, Weissig H, Shindyalov IN, Bourne PE. The Protein Data Bank. Nucleic Acids Res. 2000;28(1):235–242.

31. Salentin S, Schreiber S, Haupt VJ, Adasme MF, Schroeder M. PLIP: fully automated protein-ligand interaction profiler. Nucleic Acids Res. 2015;43(W1):W443–7.